Laser and Particle Beams (2000), *18*, 573–581. Printed in the USA.

Heavy-ion-induced hydrodynamic motion in lead targets

S. STÖWE,[1] U. NEUNER,[1] R. BOCK,[1] M. DORNIK,[1] V.E. FORTOV,[2] U.N. FUNK,[3] M. GEISSEL,[4] S. GOLUBEV,[5] D.H.H. HOFFMANN,[1,3] M. KULISH,[2] V. MINTSEV,[2] M. ROTH,[4] B. SHARKOV,[5] A. SHUTOV,[2] P. SPILLER,[1] M. STETTER,[1] W. SÜSS,[3] N.A. TAHIR,[3] A. TAUSCHWITZ,[1] AND V. YAKUSHEV[2]

[1]Gesellschaft für Schwerionenforschung Darmstadt, 64291 Darmstadt, Germany
[2]Institute for Chemical Physics Research, 142432 Chernogolovka, Russia
[3]Darmstadt University of Technology, Institute for Nuclear Physics, 64289 Darmstadt, Germany
[4]Darmstadt University of Technology, Institute for Applied Physics, 64289 Darmstadt, Germany
[5]Institute of Theoretical and Experimental Physics, 117259 Moscow, Russia

(RECEIVED 6 November 1999; ACCEPTED 31 October 1999)

Abstract

The hydrodynamic response of metal targets to volume heating by energy deposition of intense heavy-ion beams was investigated experimentally. Recent improvements in beam parameters led to a marked increase in specific deposition power: $2 \cdot 10^{10}$ $^{40}Ar^{18+}$ ions of 300 MeV/u focused to a spot size of 300 μm (σ) $\times$ 540 μm (σ) yield a specific deposition energy in solid lead of approximately 1 kJ/g in the Bragg peak, delivered within 250 ns [full width at half maximum (FWHM)]. This value allowed us for the first time to observe heavy-ion-beam-induced hydrodynamic expansion of metal volume targets. Measurements comprise expansion velocities of free surfaces of up to 290 $\pm$ 20 m/s, surface temperatures of ejected target matter of 1600–1750 K, and pressure waves in solid metal bulk targets of 0.16 GPa maximum absolute value and 0.8 μs FWHM. The experimental results agree well with the results of a 2D hydrodynamic code. Inside the interaction zone, which can only be accessed by simulation, maximum temperatures are 2800 K and maximum pressures are 3.8 GPa.

1. INTRODUCTION

Intense high-energetic heavy-ion beams are a tool well suited to generate dense plasmas (Stöckl *et al.*, 1996). The advantage of this scheme is the homogeneous coupling of beam energy into matter over a range of several millimeters. This opens up the possibility of intensely heating rather large volumes of matter at solid-state density, typically of the order of a few cubic millimeters. Experiments in fundamental research on the equation of state, phase transitions, and opacities of matter under high pressure become possible. Knowledge gained from such experiments is of considerable interest in the fields of astrophysics, geophysics, and inertial confinement fusion (Duderstadt & Moses, 1982).

In former experiments solid cryogenic rare gases, xenon, krypton (Dornik *et al.*, 1996), argon, and neon were employed as targets. Because of the low cohesive energy of these materials, hydrodynamic motion could be observed with a comparatively low deposition energy. This hydrodynamic motion in itself reveals thermodynamic properties of the matter under investigation and, additionally, it can be employed to compress other parts of the target, yielding matter above solid-state density (Arnold & Meyer-ter-Vehn, 1988; Funk *et al.*, 1998). Hydrogen under such compression is expected to undergo a phase transition to a metallic state (Wigner & Huntington, 1935). However, to reach this experimental goal, metal targets are needed to absorb the beam energy and, by subsequent expansion, compress the solid cryogenic hydrogen (Tahir *et al.*, 1998*a*, 1998*b*).

Recent improvements in ion-beam parameters now allow us to induce and observe this hydrodynamic motion in metal targets (Stöwe *et al.*, 1998). The beam parameters and the results of measurements and simulations of the target response are reported here.

As given in Section 2, the improvements in beam parameters comprise an increase in the number of ions, a reduction of the beam pulse length, and a reduction of the focal spot size. Targets and diagnostics are also described in this section.

The solid cryogenic rare gas targets' advantage of transparency for visible light, which makes them suitable for spectroscopic investigation of the beam target interaction zone, is lost for metal targets. The diagnostics for the heavy-ion-heated metal targets therefore includes time resolved 2D optical

Address correspondence and reprint requests to: U. Neuner, GSI, Planckstr. 1, D-64291 Darmstadt, Germany. E-mail: u.neuner@gsi.de

shadowgraphy to examine the hydrodynamic expansion, piezoelectric pressure gauges to detect the propagation and amplitude of pressure waves in the target, and pyrometry to measure the temperature of target matter. Results of these measurements are reported in Sections 3, 4, and 5 respectively.

In Section 6, the experimental results are compared to the results of a 2D hydrodynamic code. Results of the simulation are then evaluated not only at the points of measurement but over the whole target, including the interaction zone.

In Section 7, conclusions from the presented work are drawn and an outlook on applications of the knowledge gained is given.

2. BEAM PARAMETERS, TARGETS, AND DIAGNOSTICS

The maximum achievable number of ions per pulse in the heavy-ion synchrotron SIS at the Gesellschaft für Schwerionenforschung (GSI) Darmstadt decreases with increasing atomic number, due to restrictions in the ion sources and the first acceleration section. Conversely, the specific deposition energy per ion increases with increasing atomic number. An argon beam turned out to achieve the highest specific deposition energy in the target. The recent increase by a factor of four in the number of ions is due to the installation of the *multicusp ion source* (MUCIS) (Bossler *et al.*, 1998), which provides higher injection currents into the SIS. The maximum number of ions per pulse is $2 \cdot 10^{10}$ for a beam of $^{40}Ar^{18+}$ at an energy of 300 MeV/u.

The ions are delivered in a single bunch with a pulse length of 250 ns [full width at half maximum (FWHM)], whereas in former experiments the time structure comprised four bunches, each 80 ns (FWHM) long, with a time of 270 ns between subsequent bunches. The reduction in total pulse length is important to avoid significant expansion of the heated matter during the energy deposition. Lateral expansion, that is, decrease in density integrated over length, would lead to an increase of the ion range, thus spreading the deposited energy over a larger part of the target, decreasing the specific deposited energy. For the above-stated beam parameters this expansion is negligible. During the target heating time, which is equal to the pulse length of the beam since thermalization is several orders of magnitude faster, the density of the target stays almost constant. The ion range does not vary significantly from that in solid lead.

The absolute beam intensity and the pulse structure are recorded with fast current transformers. Figure 1 shows the recent improvements in amplitude and time structure of the argon ion-beam current.

A plasma lens (Stetter *et al.*, 1993, 1996) is used for the final focusing of the heavy-ion beam. The plasma lens provides focusing angles of up to 90 mrad. The lens aberrations are low enough so that the beam intensity distribution in the focal plane is determined by the beam emittance only. Due to the different beam emittances in the vertical and horizontal directions, the focal spot has an elliptical shape. The transverse profile is Gaussian, the beam radii are 300 μm (sigma vertical) and 540 μm (sigma horizontal). The plasma lens therefore increases the beam intensity by a factor of four compared to the optimized conventional quadrupole focusing system (Heimrich *et al.*, 1990). The beam profile in the focal plane of the lens is measured by observing the light emission of 0.2 mm thick cerium-doped quartz scintillators with a gated charge-coupled device (CCD) camera.

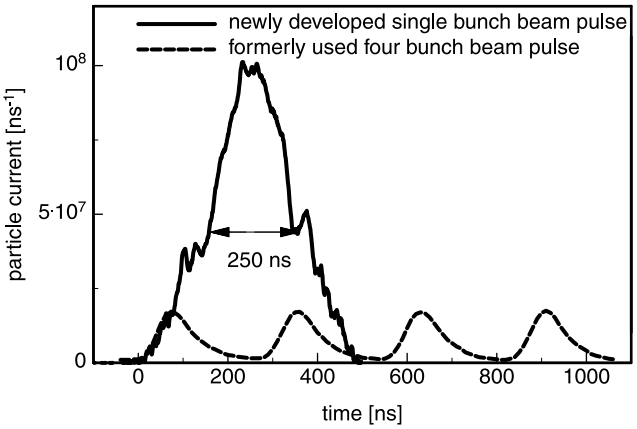

Fig. 1. Recent improvements in time structure and intensity of the beam pulse.

The spatial distribution of the specific deposition energy in the target is mainly determined by the beam envelope and the specific deposition energy of a single ion. The latter increases along the path of the ion into the target; the former is governed by the final focusing system. To calculate the specific deposition energy, initial energy spread, energy loss straggling, and angular straggling were also taken into account. Figure 2 shows the calculated longitudinal profile of

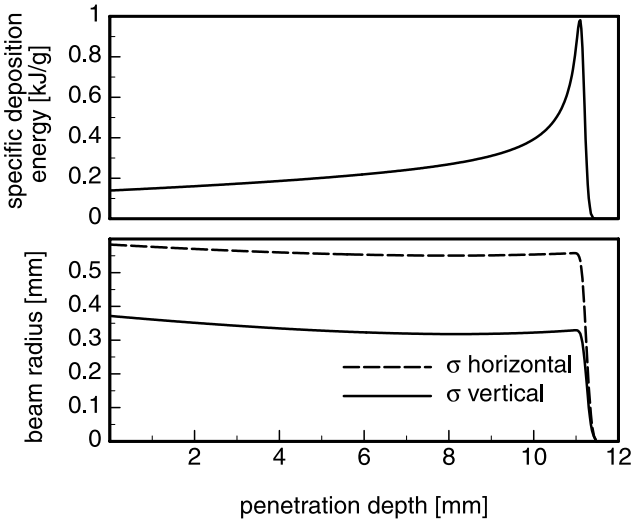

Fig. 2. Specific deposition energy along the beam axis in a lead target (top) and width of transversal beam intensity distribution (bottom) *versus* penetration depth.

https://doi.org/10.1017/S0263034600184010 Published online by Cambridge University Press

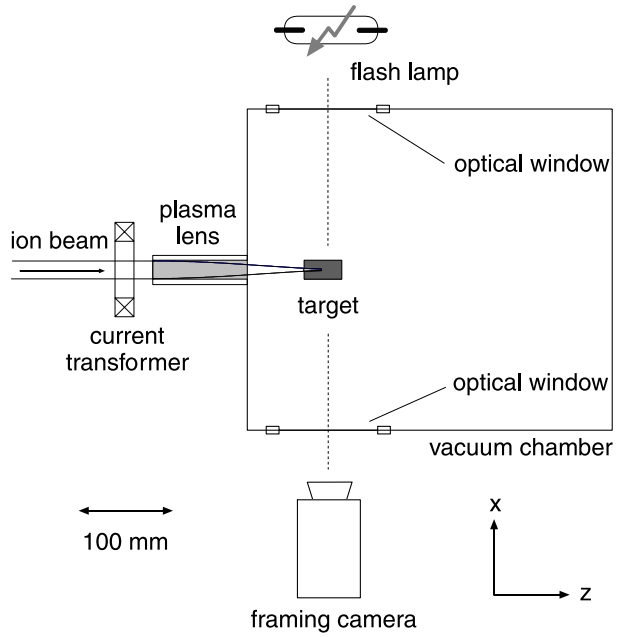

Fig. 3. Experimental setup to measure heavy-ion-induced hydrodynamic motion in lead targets.

the specific deposition energy along the beam axis assuming constant target density. In the lower part of the diagram, the beam envelope is plotted. Exploiting the enhancement of the energy deposition in the Bragg peak at the end of the ion range, the specific deposition energy in solid lead is approximately 1 kJ/g.

Figure 3 shows a sketch of the target zone with plasma lens, vacuum chamber, target and diagnostics.

Two types of targets were employed. To investigate the expansion of a free surface of heavy-ion-heated lead, the first type of target is a lead sheet of 1 mm thickness (Fig. 4a). The hydrodynamic motion of the target matter is measured with time-resolved shadowgraphy. A xenon flash lamp acts as an optical backlighter and illuminates the target from the rear side. The direction of observation (x in Fig. 3) is perpendicular to the beam direction (z) and parallel to the surface of the lead sheet. The shadow of the expanding matter is recorded with a fast multiframing camera (Coleman, 1963; ITEP, 1980), visualizing the hydrodynamic processes in 60 frames with a minimum interframing time of 1.7 μs.

The second type of target consists of a lead cylinder with implemented piezoelectric pressure gauges (Fig. 4b). The lead cylinder has a diameter of 17 mm, resulting in a large volume of matter around the interaction zone that was not directly heated in contrast to the first target configuration. The gauges are foils of polyvinylidene fluoride (PVDF) 25 μm thick (Bauer, 1981/1982; Boustie, 1996) having a square active area of 5 mm^2 and a sensitivity of 25 pC/N. Due to the thickness of the gauge, the time resolution is 10 ns. The radial distances of the gauges to the beam axis range between 3 and 6 mm. A pressure wave passing the gauge causes a current signal in the electrical circuit connected to the gauge, which is recorded as a voltage drop over a terminating resistance with a fast storage oscilloscope. The integrated signal is proportional to the pressure as a function of time. Due to the finite size of the gauges and the cylindrical geometry of the interaction process, measurements closer than 3 mm to the axis would lead to an unacceptably large error. Pressure values in the interaction zone itself can therefore only be drawn from extrapolation or simulation.

Another diagnostic used with this second type of target is pyrometry, where a fast gated camera with narrow optical-band-path filters is employed to measure the surface tem-

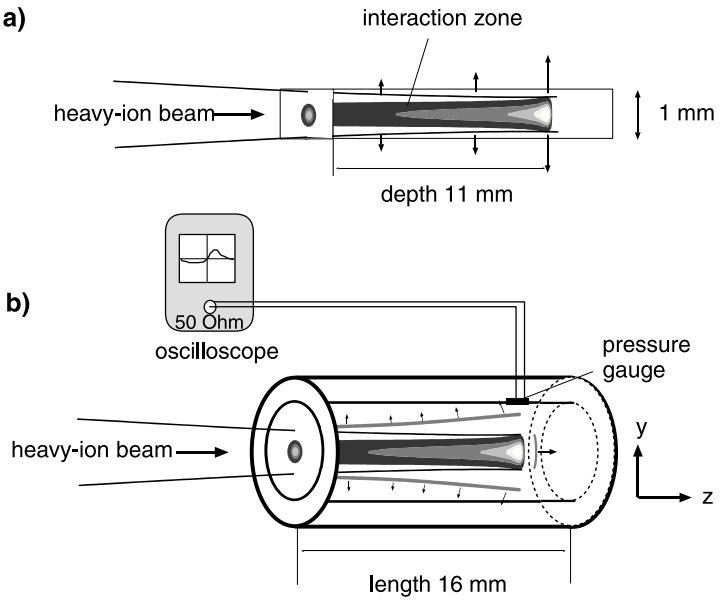

Fig. 4. Lead targets. (a) Lead sheet. (b) Lead cylinder with implemented piezoelectric pressure gauge.

https://doi.org/10.1017/S0263034600184010 Published online by Cambridge University Press

perature of target matter being ejected where the ion beam enters the target.

3. HYDRODYNAMIC MOTION OF HEAVY-ION-HEATED LEAD TARGETS

Intense heating of a lead target with a heavy-ion beam results in a hydrodynamic expansion as described below. In this experiment, the lead sheet, that is, the first target type as described in the previous section, was positioned in such a way that the focal plane of the ion beam coincided with the position of the Bragg peak inside the lead target. The beam axis lies in the midplane of the lead sheet. The results of the shadowgraphy measurement on the expansion of the target are shown as a time sequence of six frames in Figure 5. The exposure time of each frame is 3.5 μs. The expansion of the lead in the transverse direction is symmetric to the beam axis; the direction of the matter velocity is almost purely transverse. In addition there is an expansion of lead in the longitudinal direction, antiparallel to the ion beam. From frames like those in Figure 5 the velocity of the matter vacuum surface was inferred. The transverse expansion velocity is constant in time, but its absolute value is increasing in the z direction. Where the ion beam enters the target, its absolute value is 230 ± 20 m/s. At the location of the Bragg peak, it reaches a maximum of 290 ± 20 m/s. The front of the matter expanding in the longitudinal direction propagates with a velocity of 210 ± 30 m/s absolute value at the beam axis. Again, this value is constant in time.

4. PRESSURE WAVES INDUCED IN CYLINDRICAL LEAD TARGETS

Using the second target type, the large diameter lead cylinder, we measured the shape and amplitude of pressure waves that propagate from the beam-target interaction zone to outer target regions.

4.1. Variation of the distance from the sensor to the beam axis

Figure 6 shows the time development of the pressure, recorded with two gauges. Gauge 1 has a distance of 6 mm to the beam axis, gauge 2 a distance of 4 mm. Both are at a depth of 6 mm from the beam entrance plane, that is, the surface through which the ion beam enters the target. The maximum absolute values are 0.10 GPa for gauge 1 and 0.16 GPa for gauge 2. The decrease in maximum pressure with the distance from the beam axis results from the cylindrical expansion of the pressure wave. The shape of the pressure pulse is due to the temporal beam pulse structure, which is represented by the dashed curve in Figure 6 (intensity in a.u.) broadened by the spatial beam intensity profile. No shock-wave-like sharp pressure rise can be observed. The maximum of the pressure pulse propagates with 1.9 ± 0.1 km/s through the observed radial region (4–6 mm). We therefore identify the observed pressure wave with a plane elastic sound wave, the velocity of which (2.1 km/s) (Zel'dovich & Raizer, 1967) is close to the measured value. The difference between measured and theoretical velocities might be due to the fact that the experiment takes place in a pressure region where pure elastic behavior starts to be replaced by plastic behavior with an associated lower sound velocity.

4.2. Variation of the sensor position along the beam axis

Figure 7 again shows the time development of the pressure, recorded with two gauges. The gauges are located 4 and 11 mm from the beam entrance plane, respectively. Both are

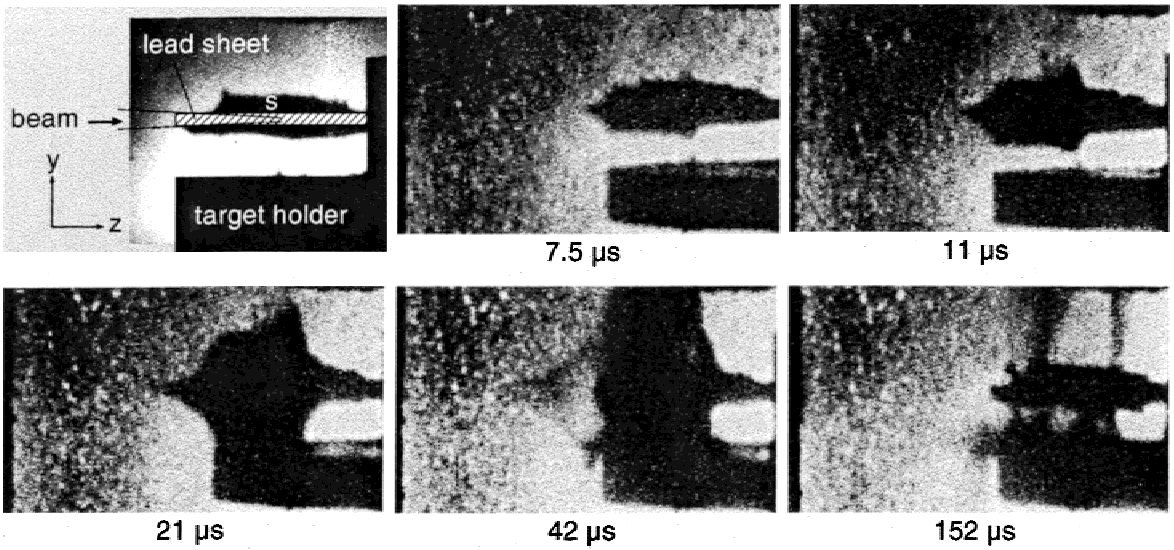

Fig. 5. Hydrodynamic expansion of a 1 mm thick lead sheet. (s: shadow of solid lead that was piled up in a previous shot at a different x position on the sheet).

https://doi.org/10.1017/S0263034600184010 Published online by Cambridge University Press

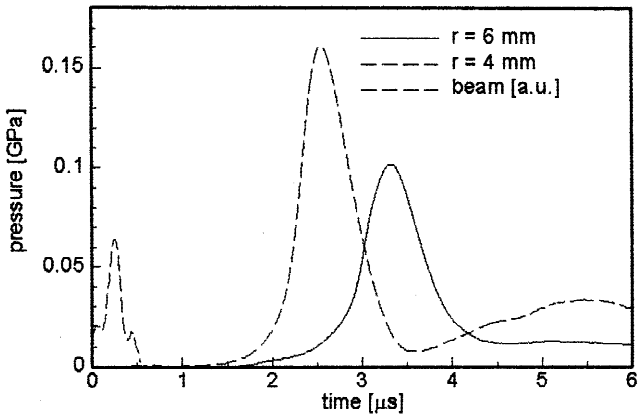

Fig. 6. Comparison of pressure measurements at different distances from the beam axis.

6.5 mm from the beam axis. The maximum absolute values are 23 and 27 MPa and the pulse widths are 1.48 and 1.25 μs. The sensor positioned 11 mm from the beam entrance plane is close to the Bragg peak where the specific deposition energy and hence the pressure reaches its maximum, so that it measures a larger pressure than the sensor 4 mm from the beam entrance plane. Following the deposition profile only, the difference in the measured maximum pressures should be much larger, but the rather small difference of 17% can be explained geometrically: In the entrance channel, the pressure wave expands cylindrically, its pressure amplitude being proportional to $r^{-0.5}$, where r is the distance from the axis, at least for large r. At the end of the range of the ion beam, close to the Bragg peak, the pressure wave expands spherically, its pressure amplitude being for large r proportional to r^{-1}, where r is the distance from the point source. The pressure wave at a depth of 11 mm from the beam entrance plane is therefore starting with a much higher amplitude than the one starting at 4 mm, but it is decaying much faster. The difference in the pulse widths is due to the difference in the transverse beam profile: The sensor at 11 mm is close to the focus, whereas in the plane of the sensor at 4 mm, the beam has a broader spatial extend, broadening the temporal pressure signal.

4.3. Comparison of plane sensor and bent sensor

In the experiments described herein the piezoelectric pressure sensors were bent to follow the cylindrical geometry. Because they were originally developed for plane applications, the effect of the bending was investigated by comparing the signals of a plane and a bent sensor. Both sensors were situated at a depth of 5 mm from the beam entrance plane; the distance from the beam axis was 3.3 mm for the plane sensor and 5.1 mm for the bent sensor. The results of this measurement is shown in Figure 8. The maximum pressure amplitude is 82 MPa for both sensors, the pulse width (FWHM) is 0.47 μs for the plane and 0.35 μs for the bent sensor. These pressure values are averages over the sensor area. Whereas for the bent sensor every part of the sensor has the same distance from the beam axis, this is not the case for the plane sensor. Its signal is therefore broadened by 70 ns, which is close to the experimental value. Following the $r^{-0.5}$ proportionality of the pressure for cylindrical waves mentioned in the preceding subsection, the pressure at the position of the plane sensor should be higher than at the position of the bent sensor by a factor of 1.2. Because of the broadening mentioned earlier, the maximum pressure of the plane sensor is lowered, so that both effects cancel each other and both sensors measure the same maximum value.

5. SURFACE TEMPERATURE OF LIQUID LEAD

When the ion beam interacts with the large diameter cylindrical type of target, a jet of liquid lead is ejected from the entrance point of the beam. It results in a cavity slightly more than 11 mm deep, with an elliptical cross section of 1.5 mm horizontal and 1 mm vertical diameter. This corre-

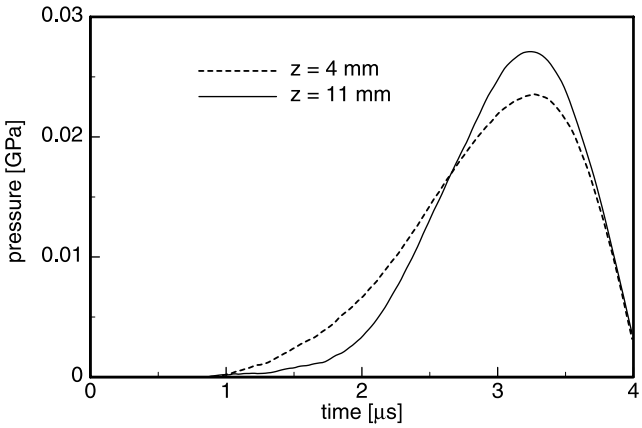

Fig. 7. Comparison of pressure measurements at different distances from the surface plane where the beam enters the target.

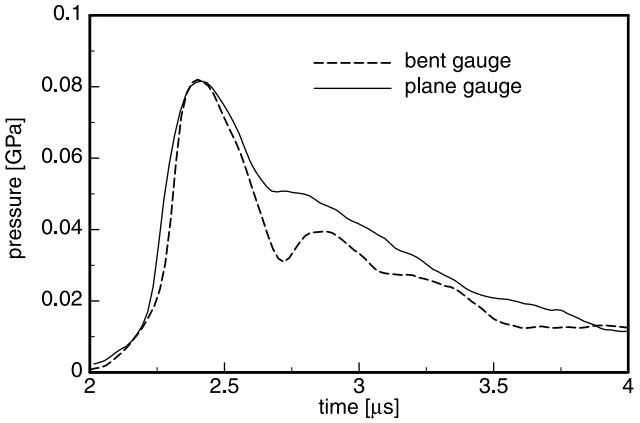

Fig. 8. Comparison of pressure measurements with a plane and a bent piezoelectric pressure gauge.

https://doi.org/10.1017/S0263034600184010 Published online by Cambridge University Press

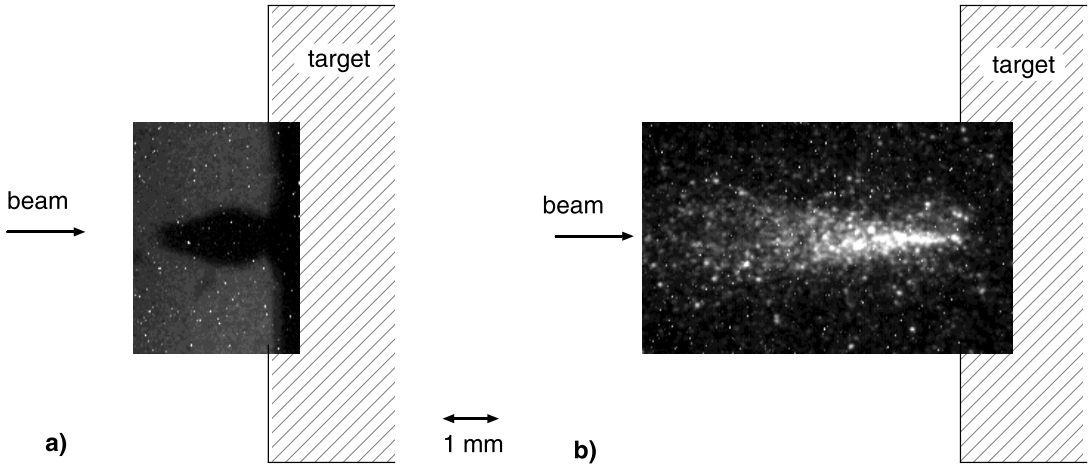

Fig. 9. Pyrometric measurement on ejected lead. (a) Jet of liquid lead ejected from a cylindrical target in time-resolved optical shadowgraphy, $t = 32$ μs. (b) Time-integrated light emission at $\lambda = 589$ nm.

sponds to the volume heated by the ion beam. The expansion of the jet in the longitudinal and vertical directions was recorded with optical shadowgraphy. Figure 9a shows an image of the backlighted target with an exposure time of 1 μs at a time of 32 μs after the beam interaction. Without use of the backlighter, a time-integrated image of the light emission of the liquid lead is obtained with an image-intensified camera, equipped with a small bandwidth (9 nm) optical filter. In Figure 9b the distribution of the light emission at 589 nm is shown. White regions correspond to high radiation densities. The brightest emission is observed close to the surface of the target. Shot-to-shot reproducibility is good when new targets are provided for each shot. Therefore a change of the filter from shot to shot enables a comparison of the light emission at different wavelengths. In Figure 10 the absolute radiation density at five different wavelengths is plotted. The optical diagnostic system was calibrated, replacing the target by a tungsten lamp with known spectral distribution of the absolute radiation density in the visible region. The measured data were fitted with a Planck curve. Taking into account the experimental error and assuming a total emission time of 15 ± 5 μs and an emissivity $\varepsilon = 1$, a surface temperature of the hottest region between 1600 K and 1750 K can be calculated.

6. COMPUTER SIMULATIONS OF THE HYDRODYNAMIC EXPANSION

The simulations are carried out with a 2D hydrodynamic code that treats interfaces with the Godunov method in moving grids (Fortov *et al.*, 1996). The code uses a semiempirical wide-range equation of state (Bushman, 1992). Beam parameters such as beam envelope, energy, and pulse shape were chosen to match the experimental conditions. The spe-

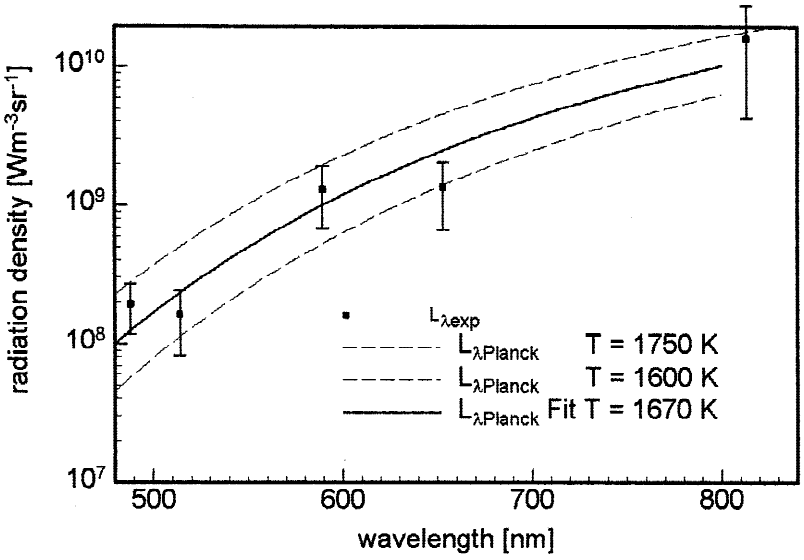

Fig. 10. Absolute spectral radiation density L_λ at five different wavelengths λ and fitted Planck curves.

https://doi.org/10.1017/S0263034600184010 Published online by Cambridge University Press

Table 1. *Expansion velocities of the surface of the lead sheet target at different distances z from the entrance point of the beam into the target*

z	5 mm	7 mm	9 mm
Simulation	0.10 km/s	0.13 km/s	0.17 km/s
Measurement	0.20 km/s	0.21 km/s	0.29 km/s

cific deposition energy is computed using stopping-power tables (Ziegler, 1985), taking into account the expansion of the matter, that is, the change in density.

To check the validity of the simulation, experiments with both types of targets were simulated and the calculated results were compared to the measured parameters. For the lead sheet targets, these were the surface velocities; for the lead cylinder targets, it was the pressure. The simulations were carried out in a plane perpendicular to the axis. For the time window of interest, the depth of this plane from the beam entrance plane of at least 4 mm is large enough that the expansion is purely transverse.

Table 1 compares the results of simulation and measurement for the expansion velocity of the target surface. Results agree for the order of magnitude of the absolute value and for the qualitative *z* dependence. Deviations can be explained by optically thick debris clouds of small liquid droplets with higher velocities than the free surface velocity.

Concerning the comparison of calculated and measured pressure in the lead cylinder targets, the data of the simulation are plotted in Figure 11. They correspond to the experimental results in Figure 6. The shape of the positive part of

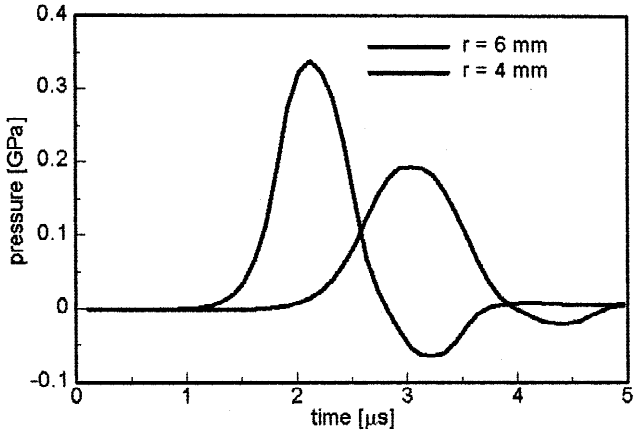

Fig. 11. Results of the simulation: pressure at the positions of the gauges, corresponding to the measurements in Figure 6.

the pressure pulse fits the experimental data well. The pulse amplitudes are 0.19 GPa for gauge 1 and 0.34 GPa for gauge 2, and thus are higher by a factor of two than in the experiment. This deviation is caused by the embedding of the gauges in a thin layer of epoxy glue. This layer of a lower acoustic impedance than lead is not taken into account in the calculation of Figure 11. Instead the simulation yields only the pressure in an infinite lead cylinder. In another experiment, where the pressure at the contact surface between lead and epoxy was measured and calculated, the simulation reproduced the measured pressure pulse amplitude within 5%. The reason for the deviation in the arrival time of the pulses is the poor accuracy in the experimental determination of the transversal gauge position with respect to the beam. In

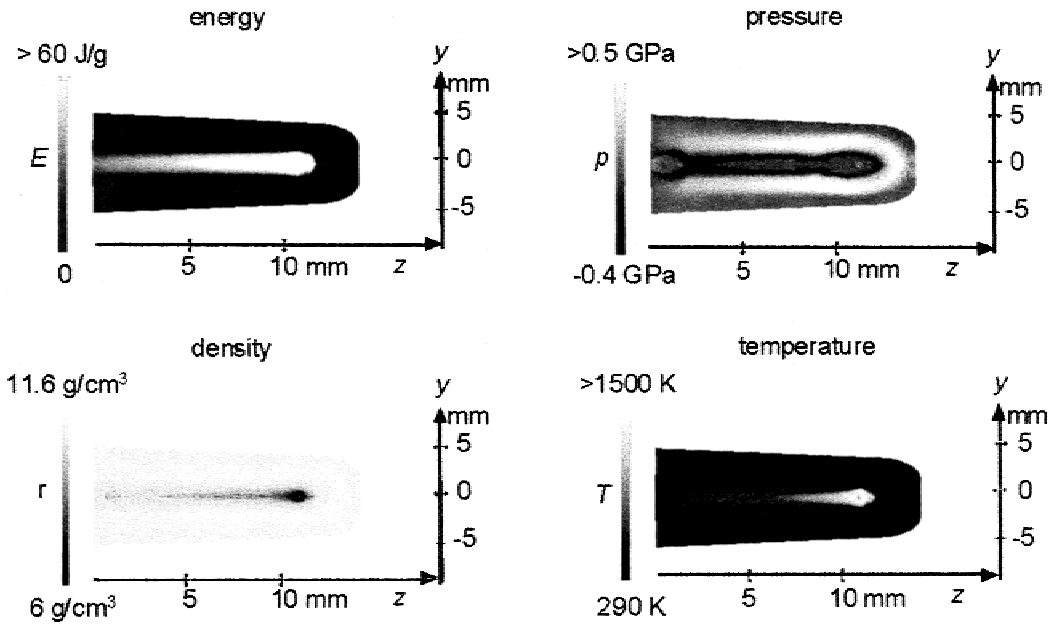

Fig. 12. Energy, pressure, density, and temperature distribution at $t = 1200$ ns, simulated with the 2D hydrodynamic code.

https://doi.org/10.1017/S0263034600184010 Published online by Cambridge University Press

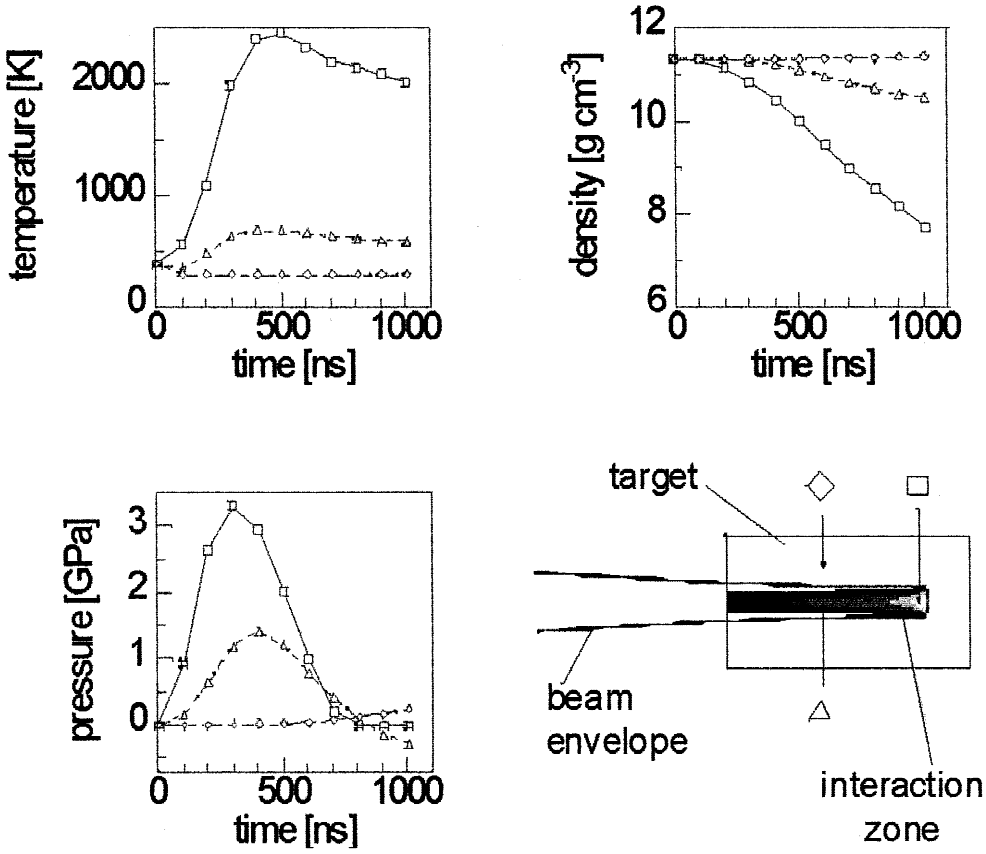

Fig. 13. Time development of temperature, density, and pressure calculated at three different positions in a cylindrical target. The beam interaction time is between 0 and 500 ns.

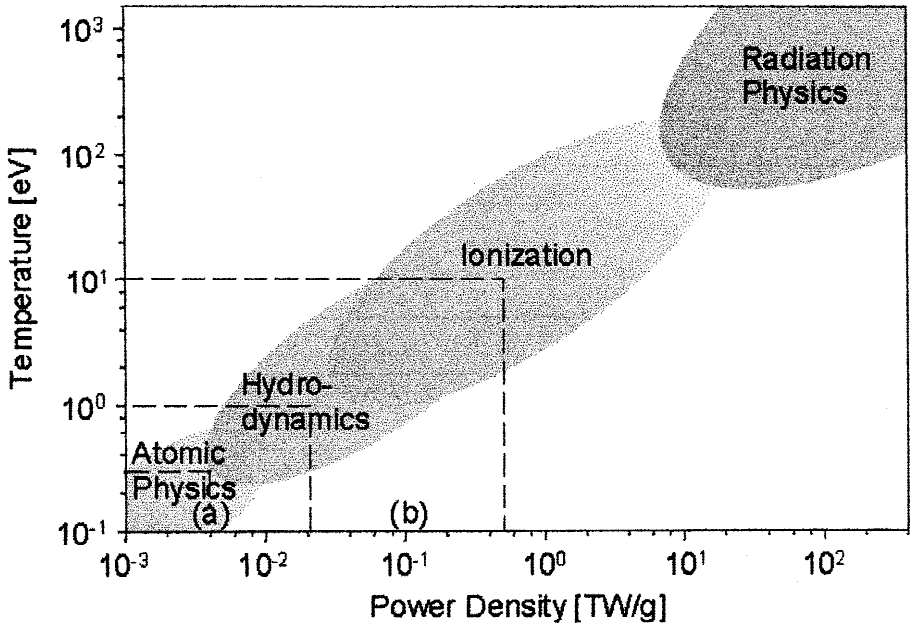

Fig. 14. Parameter region of heavy-ion-induced plasmas. (a) Experiments reported here. (b) Parameter range accessible after the high current upgrade at GSI.

https://doi.org/10.1017/S0263034600184010 Published online by Cambridge University Press

the simulation, an expansion wave with negative pressures propagates through the target behind the positive pressure pulse. This phenomenon is caused by the cohesive forces in the dense matter. It is not observed in the experiment. The current explanation might be insufficient coupling of the sensor to the lead.

Having in this way demonstrated the validity of the simulation, at least within a factor of two, the results of the simulation can be employed to extrapolate the knowledge of target parameters beyond the measured data. For this purpose, a simulation in a plane containing the beam axis was carried out. Cylindrical symmetry was assumed. Figure 12 shows energy, pressure, density, and temperature distribution in the lead target at a time of 1200 ns, which is 700 ns after the end of the heating phase. In Figure 13 the time development of the calculated temperature, density, and pressure is plotted for three specific positions in the target.

The simulation shows that the range of the ions during the heating phase is not significantly enlarged by matter dilution in the interaction zone. The maximum temperature (2800 K) and pressure (3.8 GPa) are reached at $t = 400$ ns in the center of the Bragg peak.

7. CONCLUSIONS AND OUTLOOK

The techniques for producing, measuring, and simulating heavy-ion-induced hydrodynamics in metal targets have been developed and were run successfully. The heavy-ion-beam-induced expansion of metal targets can now be applied to investigate the equation of state and transport properties of hot, expanded metals. It can, moreover, be employed to compress other materials to super-solid-state densities.

When completed in 2003, the high intensity upgrade of the GSI accelerator facilities (Braun-Munzinger *et al.*, 1997) will increase the total kinetic beam energy by two orders of magnitude to about 1 kJ. The specific deposition energy will become 100 kJ/g and temperatures between 1 eV and 10 eV at almost solid-state densities will be achievable (Müller & Spiller, 1996). Simulations showed that cylindrical compression of solid hydrogen by heavy-ion-heated lead can produce parameters where the transition to the metallic phase of hydrogen is expected (Tahir *et al.*, 1998*a*, 1998*b*). Figure 14 shows the parameter region of heavy-ion-induced dense nonideal plasmas and the different fields of physics that become achievable with increasing specific deposition power.

ACKNOWLEDGMENTS

This work was supported by the Bundesministerium für Bildung und Forschung (BMBF), the International Association for the promotion of cooperation with scientists from the independent states of the former Soviet Union (INTAS), and the Wissenschaftlich-Technische Zusammenarbeit (WTZ).

REFERENCES

Arnold, R.C. & Meyer-ter-Vehn, J. (1988). *Z. Phys. D* **9**, 65.

Bauer, F. (1981/1982). *AIP Conference Proceedings on Shock-waves in Condensed Matter* (Nellis, W.J., Ed.), 251.

Bossler, J., Emig, H., Khaouli, M., Leible, K.D., Mühle, C., Reich, H., Schulte, H., Spädtke, P. & Tinschert, K. (1998). *Report* 98-1. Darmstadt, Germany, GSI, 161.

Boustie, M. (1996). *Laser Part. Beams* **2** (14), 171.

Braun-Munzinger, P., Emling, H., Gross, K.-D. & Kluge, H.-J. (Eds.) (1997). *GSI Nachrichten* **3**, 17.

Bushman, A.V. (1992). *Intense Dynamic Loading of Condensed Matter*. Washington, DC: Taylor & Francis.

Coleman, K.R. (1963). *Repts. Progr. Phys.* **26**, 269.

Dornik, M., Dubenkov, V.P., Filimonov, A., Hoffmann, D.H.H., Kulish, M., Laux, W., Seelig, W., Sharkov, B., Spiller, P., Stetter, M., Stöckl, C., Stöwe, S., Süss, W. & Wetzler, H. (1996). *Fus. Eng. Des.* **32–33**, 511.

Duderstadt, J.J. & Moses, G.A. (1982). *Inertial Confinement Fusion*. New York: John Wiley.

Fortov, V.E, Goel, B., Munz, C.-D., Ni, A.L., Shutov, A.V. & Vorobiev, O.Yu. (1996). *Nucl. Sci. Eng.* **123**, 169.

Funk, U.N., Bock, R., Dornik, M., Geissel, M., Stetter, M., Stöwe, S., Tahir, N. & Hoffmann, D.H.H. (1998). *Nucl. Inst. Meth. A* **415**, 68.

Heimrich, B., Nestle, H., Winkler, M., Hoffmann, D.H.H. & Wollnik, H. (1990). *Nucl. Instr. Meth. A* **294**, 602.

ITEP (1980). *Operation Manual of the VFU-1 Camera*. Moscow: ITEP (in Russian).

Müller, R.W. & Spiller, P. (1996). *Report* 96-07. Darmstadt, Germany: GSI.

Stetter, M., Christiansen, J., Neuner, U., Stöwe, S., Tkotz, R., Wagner, T., Boggasch, E., Tauschwitz, A., Hoffmann, D.H.H. & Spiller, P. (1993). *Il Nuovo Cimento* **106 A**(11), 1725.

Stetter, M., Neuner, U., Stöwe, S., Dornik, M., Hoffmann, D.H.H., Kowalewicz, R., Spiller, P. & Tauschwitz, A. (1996). *Fus. Eng. Des.* **32–33**, 503.

Stöckl, C., Boine-Frankenheim, O., Roth, M., Süss, W., Wetzler, H., Seelig, W., Kulish, M., Dornik, M., Laux, W., Spiller, P., Stetter, M., Stöwe, S., Jacoby, J. & Hoffmann, D.H.H. (1996). *Laser Part. Beams* **14** (4), 561.

Stöwe, S., Bock, R., Dornik, M., Spiller, P., Stetter, M., Fortov, V.E., Mintsev, V., Kulish, M., Shutov, A., Yakushev, V., Sharkov, B., Golubev, S., Bruynetkin, B., Funk, U.N., Geissel, M., Hoffmann, D.H.H. & Tahir, N.A. (1998). *Nucl. Inst. Meth. A* **415**, 61.

Tahir, N.A., Hoffmann, D.H.H., Maruhn, J.A., Lutz, K.-J. & Bock, R. (1998*a*). *Phys. Plasmas* **5**(12), 4426.

Tahir, N.A., Hoffmann, D.H.H., Maruhn, J.A., Lutz, K.-J. & Bock, R. (1998*b*). *Phys. Lett. A* **249**, 489.

Wigner, E. & Huntington, H.B. (1935). *J. Chem. Phys.* **3**, 764.

Zel'dovich, Ya.B. & Raizer, Yu.P. (1967). *Physics of Shock-waves and High-Temperature Hydrodynamic Phenomena II*. New York: Academic Press, 698.

Ziegler, J.F. (1985). *The Stopping and Range of Ions in Matter*, Vol. 1. Oxford: Pergamon.